

Article

Oxygen Vacancy and Valence Band Structure of $\text{Ba}_{0.5}\text{Sr}_{0.5}\text{Fe}_{1-x}\text{Cu}_x\text{O}_{3-\delta}$ ($x = 0-0.15$) with Enhanced ORR Activity for IT-SOFCs

Taeheun Lim, Kanghee Jo and Heesoo Lee *

School of Materials Science and Engineering, Pusan National University, Busan 46241, Republic of Korea; taeheunlim@pusan.ac.kr (T.L.); jokanghee@pusan.ac.kr (K.J.)

* Correspondence: heesoo@pusan.ac.kr; Tel.: +82-51-510-2388; Fax: +82-51-512-0528

Abstract: The oxygen reduction reaction (ORR) activity of a Cu-doped $\text{Ba}_{0.5}\text{Sr}_{0.5}\text{FeO}_{3-\delta}$ ($\text{Ba}_{0.5}\text{Sr}_{0.5}\text{Fe}_{1-x}\text{Cu}_x\text{O}_{3-\delta}$, BSFCux, $x = 0, 0.05, 0.10, 0.15$) perovskite cathode was investigated in terms of oxygen vacancy formation and valence band structure. The BSFCux ($x = 0, 0.05, 0.10, 0.15$) crystallized in a cubic perovskite structure ($Pm\bar{3}m$). By thermogravimetric analysis and surface chemical analysis, it was confirmed that the concentration of oxygen vacancies in the lattice increased with Cu doping. The average oxidation state of B-site ions decreased from 3.583 ($x = 0$) to 3.210 ($x = 0.15$), and the valence band maximum shifted from -0.133 eV ($x = 0$) to -0.222 eV ($x = 0.15$). The electrical conductivity of BSFCux increased with temperature because of the thermally activated small polaron hopping mechanism showing a maximum value of 64.12 S cm^{-1} ($x = 0.15$) at 500 °C. The ASR value as an indicator of ORR activity decreased by 72.6% from 0.135 Ω cm^2 ($x = 0$) to 0.037 Ω cm^2 ($x = 0.15$) at 700 °C. The Cu doping increased oxygen vacancy concentration and electron concentration in the valence band to promote electron exchange with adsorbed oxygen, thereby improving ORR activity.

Keywords: $\text{Ba}_{0.5}\text{Sr}_{0.5}\text{Fe}_{1-x}\text{Cu}_x\text{O}_{3-\delta}$; oxygen vacancy; valence band; oxygen reduction reaction; area-specific resistance



Citation: Lim, T.; Jo, K.; Lee, H.

Oxygen Vacancy and Valence Band Structure of $\text{Ba}_{0.5}\text{Sr}_{0.5}\text{Fe}_{1-x}\text{Cu}_x\text{O}_{3-\delta}$ ($x = 0-0.15$) with Enhanced ORR Activity for IT-SOFCs. *Materials* **2023**, *16*, 3231. <https://doi.org/10.3390/ma16083231>

Academic Editor: Michał Mosialek

Received: 24 March 2023

Revised: 12 April 2023

Accepted: 18 April 2023

Published: 19 April 2023



Copyright: © 2023 by the authors. Licensee MDPI, Basel, Switzerland. This article is an open access article distributed under the terms and conditions of the Creative Commons Attribution (CC BY) license (<https://creativecommons.org/licenses/by/4.0/>).

1. Introduction

One of the important challenges for the commercialization of solid oxide fuel cells (SOFCs) is to lower the operating temperature to an intermediate temperature (IT) range of $500-800$ °C [1]. The intermediate operating temperature increases the polarization resistance of conventional cathodes like $\text{La}_{1-x}\text{Sr}_x\text{MnO}_3$, resulting in reduced electrochemical activity of the cathode for the oxygen reduction reaction (ORR). To solve this problem, cobalt-based oxides with mixed ionic-electronic conductivity (MIEC) have been studied as potential cathode materials for IT-SOFCs [2–4]. However, cobalt-based oxides have disadvantages, such as high thermal expansion coefficients (TECs), because of the flexible redox behavior of cobalt and easy evaporation and reduction of cobalt [5,6]. Therefore, developing cobalt-free cathodes with a good ORR activity for IT-SOFCs is needed.

Among the iron-based cathode materials, the cubic $\text{BaFeO}_{3-\delta}$ (BFO) materials exhibit good oxygen–electron mixed conduction and excellent chemical and thermal stabilities compared with those of cobalt-based materials [7]. The cubic BFO exhibits high oxygen ion conductivity due to the existence of disordered oxygen vacancies and three-dimensional oxygen diffusion pathways [8]. For stabilization of the BFO cubic phase, the A-site was doped with Sr, La, Ce, etc., and $\text{Ba}_{0.5}\text{Sr}_{0.5}\text{FeO}_{3-\delta}$ (BSF) achieved high electronic conductivity [9–11]. In addition, the relatively low oxygen reduction reaction rate of $\text{Ba}_{0.5}\text{Sr}_{0.5}\text{FeO}_{3-\delta}$ can be improved by substituting Fe with other transition metals to promote oxygen inflow and oxygen ion transport [12].

Replacing cations with lower valences ($2+/3+$) for $\text{Fe}^{3+/4+}$ cations can form more oxygen vacancies, which can enhance the ORR activity. For this purpose, some researchers

have doped Ni, Gd, etc., at the Fe site, and perovskite cubic materials substituted with B-sites such as $\text{BaFe}_{0.75}\text{Ni}_{0.25}\text{O}_{3-\delta}$ and $\text{BaF}_{1-x}\text{Gd}_x\text{O}_{3-\delta}$ provided high ORR activity [13,14]. Yin et al. and Lu et al. improved the electrochemical property of $\text{Pr}_{0.5}\text{Sr}_{0.5}\text{Fe}_{0.8}\text{Cu}_{0.2}\text{O}_{3-\delta}$ and $\text{Nd}_{0.5}\text{Sr}_{0.5}\text{Fe}_{0.8}\text{Cu}_{0.2}\text{O}_{3-\delta}$ by doping Cu into the Fe site [15,16]. In addition, studies on doping Cu with Ni sites have been conducted to improve electrochemical properties. Niemczyk et al. synthesized $\text{LaNi}_{1-x}\text{Cu}_x\text{O}_{3-\delta}$ series, and $\text{LaNi}_{0.5}\text{Cu}_{0.5}\text{O}_{3-\delta}$ showed a low polarization resistance of $0.056 \Omega \text{ cm}^2$ at 800°C and a relatively high power density output of 870 mW cm^{-2} at 900°C [17]. Jakub et al. studied $\text{La}_{1-x}\text{Sr}_x\text{Ni}_{1-y}\text{Cu}_y\text{O}_{3-\delta}$ and achieved the maximum power value of 450 mW cm^{-2} at 650°C [18]. Considering that Cu is present in multiple oxidation states (Cu^+ , Cu^{2+} , Cu^{3+}), similar to Co, Fe, and Mn, it is reasonable to use perovskite materials containing Cu as the SOFC cathode [19].

The mechanism of ORR at the SOFC cathode surface involves four steps, including diffusion and adsorption of oxygen molecules, dissociation of the oxygen molecules to form oxygen atoms, lattice mixing of oxygen ions, and movement of the oxygen ions to the electrode/electrolyte interface [20]. However, the rate-determining step is not well understood because of the complex characteristics of the cathode materials, such as electronic structure and defect structure. Previous studies have suggested descriptors that can predict the ORR activity. Hardin et al. explained that the total number of valence electrons is a descriptor for ORR activity, and Jung et al. predicted the ORR activity by comparing d-band centers with the surface composition and morphology of $\text{PtCu}_x/\text{Pt}/\text{C}$ catalysts [21,22]. Additionally, Zhu et al. investigated the relationship between the polarization resistance and the valence band of LSCO thin film consisting of Co 3d and O 2p bands [23].

In this study, $\text{Ba}_{0.5}\text{Sr}_{0.5}\text{Fe}_{1-x}\text{Cu}_x\text{O}_{3-\delta}$ perovskite cathode materials were investigated to confirm the relationship between the change in the valence band structure according to Cu doping and ORR activity. The change in oxygen vacancy concentration of BSFCu_x according to Cu doping was confirmed through thermogravimetric analysis (TGA) and X-ray photoelectron analysis (XPS). In addition, the oxidation state and the valence band structure were analyzed using XPS and the polarization resistance of BSFCu_x was calculated as an indication for change in ORR activity via the impedance spectrum.

2. Experimental Procedures

2.1. Synthesis

$\text{Ba}_{0.5}\text{Sr}_{0.5}\text{Fe}_{1-x}\text{Cu}_x\text{O}_{3-\delta}$ (BSFCu_x, $x = 0, 0.05, 0.10, 0.15$) powders were synthesized by a solid-state reaction using BaCO_3 (99.0% purity, Sigma-Aldrich, St. Louis, MO, USA), SrCO_3 (99.9% purity, Sigma-Aldrich), Fe_2O_3 (99.0% purity, Sigma-Aldrich), and CuO (99.0% purity, Sigma-Aldrich) as starting materials. After mixing each material according to the stoichiometric ratio, it was ball milled together in a polyethylene container with ethanol and zirconia balls for 24 h and dried at 100°C for 12 h. The green bodies were prepared using dried powder by uniaxial compression under hydraulic pressure of 20 MPa; the green body of BSF was calcined at 1100°C for 10 h, and the green bodies of BSFCu_x ($x = 0.05, 0.10, 0.15$) were calcined at 950°C for 10 h. These calcined green bodies were ground using a mortar and sieved using a mesh of $250 \mu\text{m}$. Finally, BSFCu_x powder was synthesized by repeating the calcining, grounding, and sieving process twice.

2.2. Characterization

The crystal structure of the synthesized powders was analyzed using powder X-ray diffraction (PXRD, X'pert PRO-MPD, $\lambda = 1.54 \text{ \AA}$) in the 2θ range of $20\text{--}80^\circ$ with a step scan procedure ($0.02^\circ/2\theta$ step, 1° min^{-1}) at room temperature. The structure parameters were obtained by analyzing XRD data with Rietveld refinement (PANalytical X'Pert HighScore Plus software, version 3.0c(3.0.3)). The line shapes of the diffraction peaks were generated by a pseudo-Voigt function and the background refined to a 4th degree polynomial.

In order to determine the temperature of oxygen vacancy formation and weight reduction of BSFCu_x, thermogravimetric analysis (TGA) was carried out on a thermal analyzer (NETSCH STA 409 PC/PG) with about 100 mg of BSFCu_x powders measured

in a nitrogen atmosphere at a heating rate of $5\text{ }^{\circ}\text{C min}^{-1}$. According to the TGA data, the changes in oxygen non-stoichiometry (δ) for the powder samples were calculated using the following equation [24]:

$$\delta = \delta_0 + \frac{M_0}{15.99} \left(1 - \frac{m}{m_0}\right) \quad (1)$$

where δ_0 is the oxygen non-stoichiometry at room temperature, M_0 is the molar mass of the samples with non-stoichiometry δ_0 , 15.99 is the atomic weight of oxygen atoms, m is the final weight of the samples under various temperatures, and m_0 is the initial weight of the samples. The δ_0 was calculated by electroneutrality condition with X-ray photoelectron spectroscopy (XPS, Thermo Fisher Scientific, Waltham, MA, USA) data [25–28]. XPS was used to analyze changes in oxidation state, oxygen non-stoichiometry, and valence band structure. The spectra were calibrated using the C1s line (BE = 284.6 eV).

The electrical conductivity of BSFCu x was evaluated using the 4-probe DC technique in the range of 300–900 $^{\circ}\text{C}$, and Pt wires were wrapped around the sintered bars with dimensions of $5 \times 3 \times 30\text{ mm}^3$. A direct current of 50 mA was supplied from a current source (Keithley 2400, Solon, OH, USA), and the corresponding voltage drop was collected using a multimeter (Agilent, 34401A, Santa Clara, CA, USA).

The microstructure of the BSFCu0.15|SDC|BSFCu0.15 symmetric cell was observed using a scanning electron microscope (SEM, MIRA3, TESCAN). The area-specific resistance (ASR) of symmetrical cells of BSFCu x electrodes was measured by AC impedance spectroscopy. For an impedance analysis, a dense disk of SDC (20 mol% Samarium doped ceria, Fuelcell materials, 20 mm diameter and 600 μm thick) was used as an electrolyte. BSFCu x powder was mixed with a vehicle (Fuel Cell Materials) to prepare BSFCu x pastes using a three-roll mill, and these pastes were screen-printed on both sides of the SDC pellets with an area of 0.2826 cm^2 . After drying, the symmetric cells were calcined at 900 $^{\circ}\text{C}$ for 2 h in air to improve the adhesion between the electrolyte and the electrode. Electrochemical impedance spectra (EIS) were obtained using Iviumstat (Ivium, Netherlands) equipment, and a 10 mV excitation voltage was applied in the frequency range of 10^6 – 10^{-2} Hz at 700 $^{\circ}\text{C}$. The obtained EIS data were fitted using Zview software version 3.0.

3. Results and Discussion

Figure 1a shows the room temperature XRD patterns of the BSFCu x ($x = 0, 0.05, 0.10, 0.15$) powder, and no secondary phases appeared in the patterns, which confirmed that 0–15 mol% of Cu was stably dissolved in the BSF lattice. As shown in Figure 1b, the 2θ value of (110) peak shifted to a smaller angle as the Cu doping increased, which indicated an expansion of the lattice volume due to the larger ionic radii of Cu^+ (0.77 \AA) and Cu^{2+} (0.73 \AA) than those of Fe^{3+} (0.645 \AA) and Fe^{4+} (0.585 \AA). The XRD patterns show that BSFCu x crystallizes into a cubic perovskite structure with a space group $Pm\bar{3}m$ (Figure 2). The structural parameters calculated by Rietveld refinement are listed in Table 1, and the lattice volume increased from 61.0699 \AA^3 ($x = 0$) to 61.4428 \AA^3 ($x = 0.15$) with the Cu content.

Thermogravimetric analysis was carried out to confirm the effect of Cu doping on oxygen vacancy formation. Figure 3a shows the TG curve of the BSFCu x samples from 25 to 950 $^{\circ}\text{C}$ and Figure 3b shows the oxygen content of the BSFCu x samples using room-temperature oxygen non-stoichiometry (δ_0) from the XPS analysis. In order to more clearly observe the oxygen vacancy formation according to the Cu content, it was measured in an inert atmosphere using nitrogen gas. There were weight losses of less than 1% during heating before the slope changing point, which is due to the desorption of physically and chemically adsorbed water and other gases [29]. The slope changing temperature decreased from 500 $^{\circ}\text{C}$ ($x = 0$) to 450 $^{\circ}\text{C}$ ($x = 0.15$) and the lower slope changing temperature indicated the easier loss of oxygen in the BSFCu0.15 lattice with increasing temperature. The weight loss after the slope changing temperature increased from 1.72% ($x = 0$) to 2.09% ($x = 0.15$). The weight loss observed within this temperature range is due to the loss of lattice oxygen, indicating that the amount of oxygen vacancy in the lattice increases with Cu doping [28].

The X-ray photoelectron spectroscopy (XPS) analysis was performed to characterize the surface chemical bonding state of the BSFCu_x samples. Figure 4a–c show the Cu 2p_{3/2}, Fe 2p_{3/2}, and O 1s XPS spectra for each BSFCu_x composition and the area ratios of peaks are summarized in Table 2. The Cu 2p_{3/2} peak was deconvoluted into two peaks at approximately 932.3 eV (Cu⁺) and 934.1 eV (Cu²⁺), as shown in Figure 4a [30]. The Fe 2p_{3/2} peak was deconvoluted into 709.1 eV (Fe³⁺) and 710.8 eV (Fe⁴⁺) peaks, and a weak satellite shake-up peak was observed in the range of 715 eV to 720 eV, as shown in Figure 4b [31]. The average oxidation states of the B-site ions (Fe and Cu) are 3.583 (x = 0), 3.464 (x = 0.05), 3.332 (x = 0.10), and 3.210 (x = 0.15). Assuming an oxidation state of 2⁺ for Ba and Sr, the room-temperature oxygen non-stoichiometry (δ_0) was calculated according to the electroneutrality condition, and the oxygen non-stoichiometry increased from 0.21 (x = 0) to 0.39 (x = 0.15) as the Cu doping increased (Table 2). It is thought that the BSFCu_{0.15} cathode will enhance the catalytic activity of the ORR because the value of δ_0 indicates the amount of oxygen vacancies in the lattice.

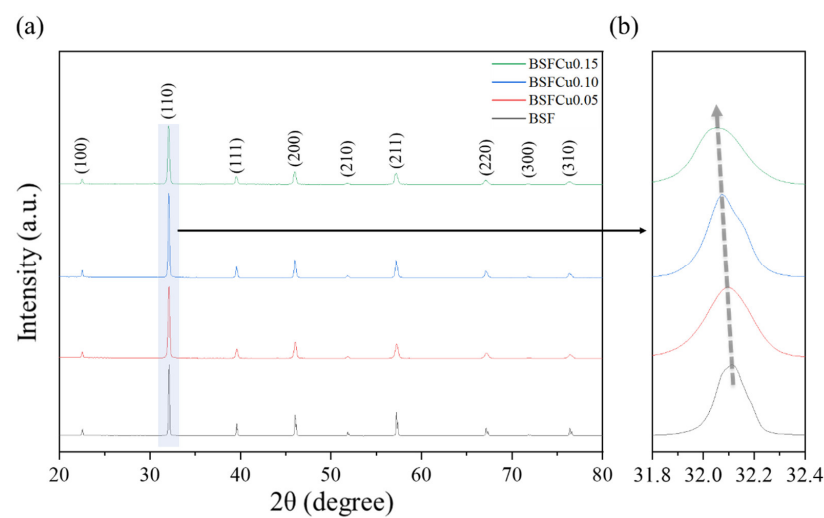


Figure 1. (a) Room temperature PXRD patterns of the Ba_{0.5}Sr_{0.5}Fe_{1-x}Cu_xO_{3- δ} (x = 0, 0.05, 0.10, 0.15). (b) Enlarged (110) peaks.

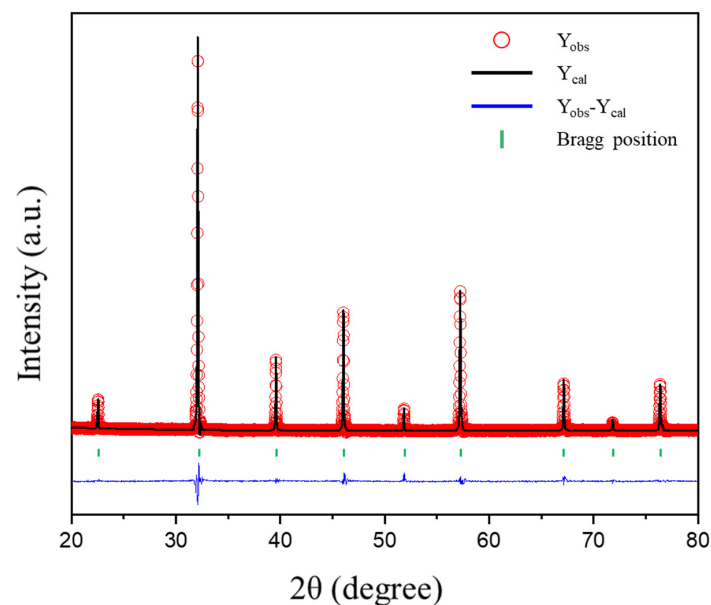
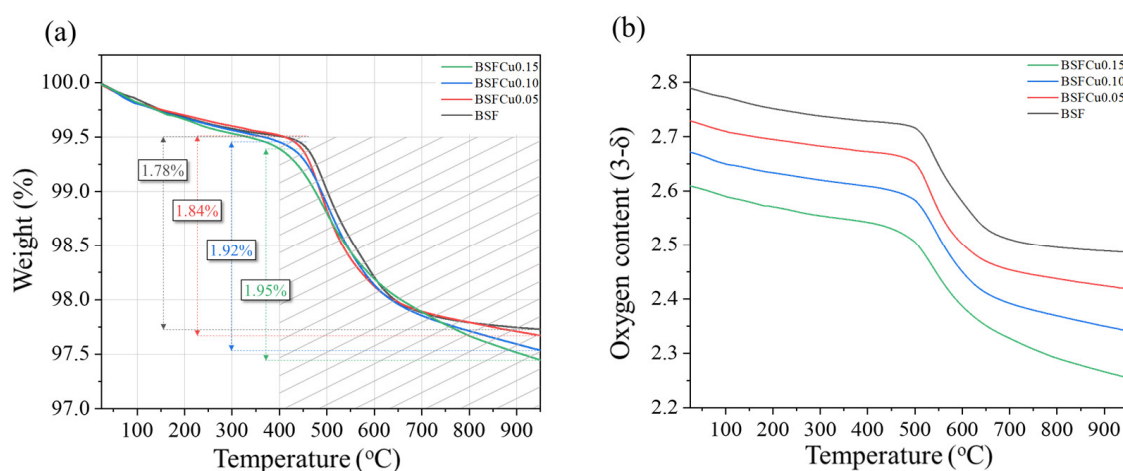


Figure 2. Rietveld refinement result of the Ba_{0.5}Sr_{0.5}Fe_{0.85}Cu_{0.15}O_{3- δ} after calcination at 950 °C for 10 h in air. The open symbol is observed intensities, the black line is calculated intensities, the blue line is the difference between the observed and the calculated intensities, and green vertical bars are Bragg positions.

Table 1. Structural parameters of the $\text{Ba}_{0.5}\text{Sr}_{0.5}\text{Fe}_{1-x}\text{Cu}_x\text{O}_{3-\delta}$ ($x = 0, 0.05, 0.10, 0.15$) calculated by Rietveld refinement of the room-temperature XRD data.

Parameters	Composition			
	BSF	BSFCu0.05	BSFCu0.10	BSFCu0.15
$a = b = c$ [Å]	3.938(6)	3.940(4)	3.943(7)	3.946(5)
Volume [Å ³]	61.0699(9)	61.1630(1)	61.3028(6)	61.4428(3)
Space group	$Pm\bar{3}m$	$Pm\bar{3}m$	$Pm\bar{3}m$	$Pm\bar{3}m$
R_{wp} [%]	6.285	7.211	7.412	6.568
R_{exp} [%]	3.792	3.281	3.414	3.364
χ^2	2.747	4.832	4.715	3.811

**Figure 3.** (a) Weight change and (b) oxygen content curves of the $\text{Ba}_{0.5}\text{Sr}_{0.5}\text{Fe}_{1-x}\text{Cu}_x\text{O}_{3-\delta}$ ($x = 0, 0.05, 0.10, 0.15$).

In Figure 4c, the O 1s peak was deconvoluted into three peaks of 527.9 eV, 530.7 eV, and 533 eV corresponding to lattice oxygen (O_{lat}), adsorbed oxygen (O_{ads}), and surface moisture (O_{moi}), respectively [32]. The adsorbed oxygen is released easily from the surface of the crystal lattice with increasing temperature, which leads to the oxygen vacancy formation. Therefore, the area ratio of O_{ads} to O_{lat} ($\text{O}_{\text{ads}}/\text{O}_{\text{lat}}$) can be used as a criterion to evaluate the relative content of oxygen vacancies in materials [33,34]. The $\text{O}_{\text{ads}}/\text{O}_{\text{lat}}$ were 1.54 ($x = 0$), 1.60 ($x = 0.05$), 1.62 ($x = 0.10$), and 1.65 ($x = 0.15$), which increased with the amount of Cu doping. It can be interpreted that BSFCu0.15 has the highest oxygen vacancy concentration among the BSFCux ($x = 0, 0.05, 0.10, 0.15$) in the intermediate temperature region, which corresponds with the thermogravimetric results (Figure 3a,b).

The valence band (VB) spectra of BSFCux are shown in Figure 5, and the peak of the Ba 5p (10.5–15.0 eV) and Sr 4p–O 2s bond (16–21 eV) was confirmed [35]. The range of 0–7.5 eV is made up of Fe 3d (1.8 eV), Cu 3d (3.1 eV), and O 2p orbitals (5.0 eV), which is closely related to the BO_6 structure. The Cu 3d area increased with an increase in Cu doping, leading to a negative shift in the valence band maximum (VBM) from -0.133 eV (BSF) to -0.222 eV (BSFCu0.15), as shown in Figure 5b. The negative shift of the VBM value represents that electron transport to the adsorbed oxygen is improved because of the increased electron concentration in the VB of BSFCux, which is expected to enable faster oxygen exchange.

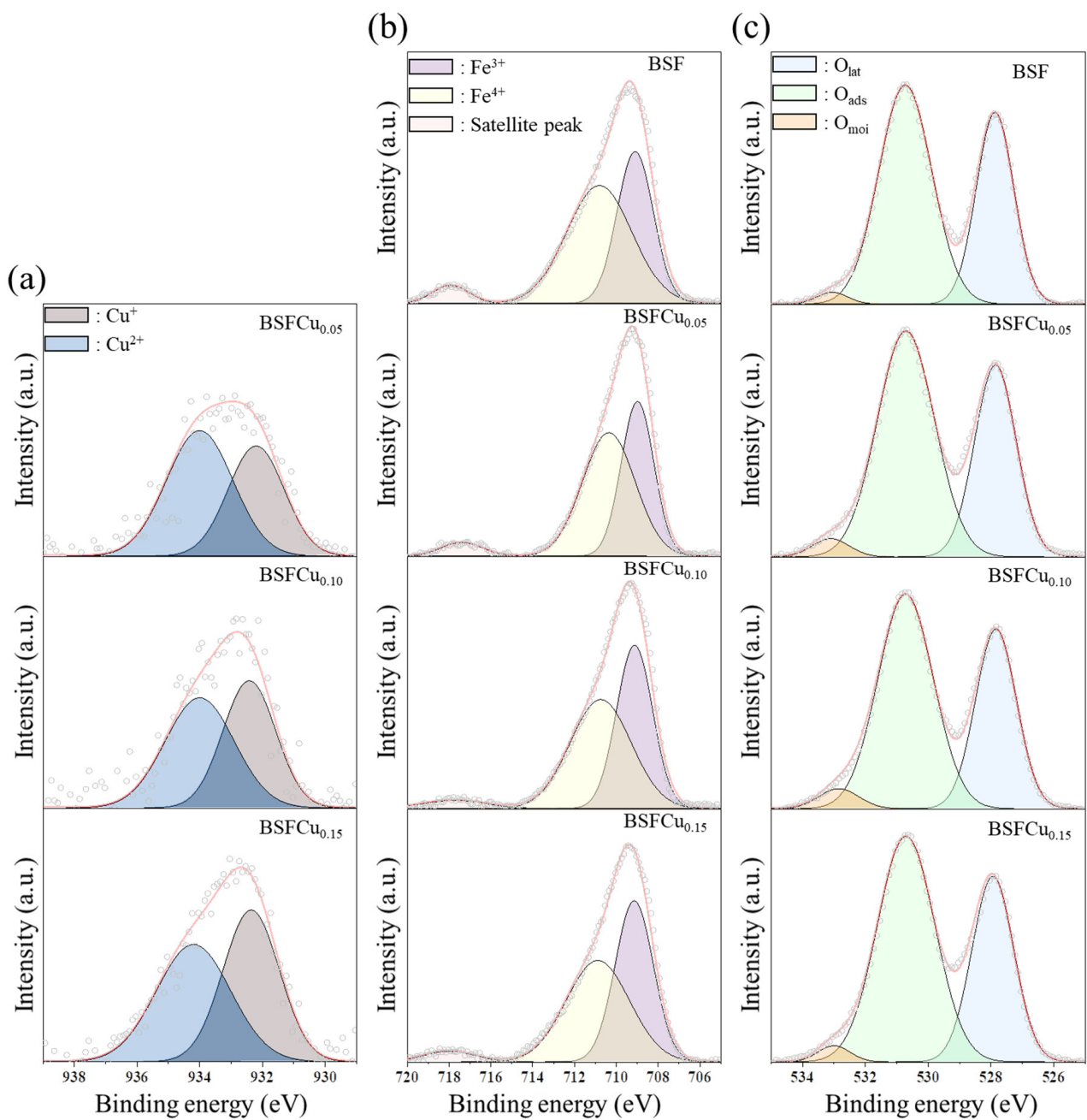


Figure 4. (a) Cu 2p_{3/2}, (b) Fe 2p_{3/2}, and (c) O 1s XPS spectra of the Ba_{0.5}Sr_{0.5}Fe_{1-x}Cu_xO_{3-δ} (x = 0, 0.05, 0.10, 0.15). The circles are the experimental data, the red line is the fitting curve.

Table 2. Fitting results of the Fe 2p_{3/2}, Cu 2p_{3/2}, and O 1s XPS spectra of the Ba_{0.5}Sr_{0.5}Fe_{1-x}Cu_xO_{3-δ} (x = 0, 0.05, 0.10, 0.15).

Sample	Fe ³⁺ (%)	Fe ⁴⁺ (%)	Cu ⁺ (%)	Cu ²⁺ (%)	Average Oxidation State	δ ₀	O _{lat} (%)	O _{ads} (%)	O _{moi} (%)	O _{ads} /O _{lat}
BSF	41.7	58.3	-	-	+3.583	0.21	38.6	59.5	1.9	1.54
BSFCu0.05	43.7	56.3	42.6	57.4	+3.464	0.27	37.3	59.6	3.1	1.60
BSFCu0.10	46.8	53.2	46.9	53.1	+3.332	0.33	36.7	59.5	3.8	1.62
BSFCu0.15	48.9	51.1	49.5	50.5	+3.210	0.39	36.6	60.3	3.1	1.65

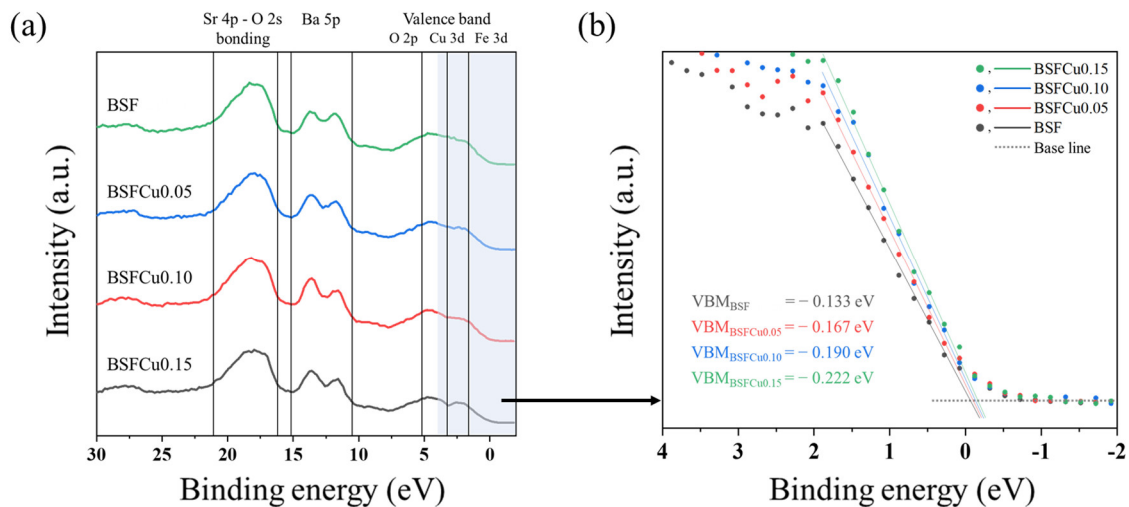
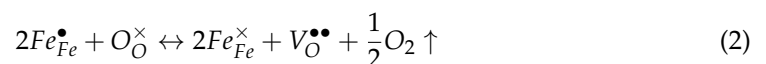


Figure 5. (a) Valence band (VB) spectra normalized to the integrated intensity for BSFCu_x; (b) linear fit of the leading edge of VB used to obtain the valence band maximum (VBM).

Fe-based perovskite oxides show mixed ionic-electronic conductivity (MIEC) because of the simultaneous presence of oxygen vacancies and electron holes as charge carriers. However, since the electrical conductivity is about two orders of magnitude higher than the ionic conductivity, the conductivity data of Figure 6 mainly represent the electronic conductivity [15,36]. The electrical conductivity (σ) of BSFCu_x was measured in air at 300–950 °C using the 4-probe DC technique (Figure 6a). The electrical conductivity of BSFCu_x increased with temperature and reached a maximum at 500 °C with 64.12 S cm⁻¹ ($x = 0.15$). This semiconducting behavior can be explained by a thermally activated small polaron hopping mechanism [37]. The decrease in electrical conductivity is related to the breakdown of (Fe, Cu)–O–(Fe, Cu) bonds above 500 °C because the oxygen vacancies are formed and the charge carrier concentration is reduced due to the reduction in Fe⁴⁺ (Equation (2)), which is in good agreement with the thermogravimetric results [38].



where Fe_{Fe}^{\bullet} and Fe_{Fe}^{\times} represent the Fe⁴⁺ and Fe³⁺, O_O^{\times} and $V_O^{\bullet\bullet}$ represent the lattice oxygen and oxygen vacancy.

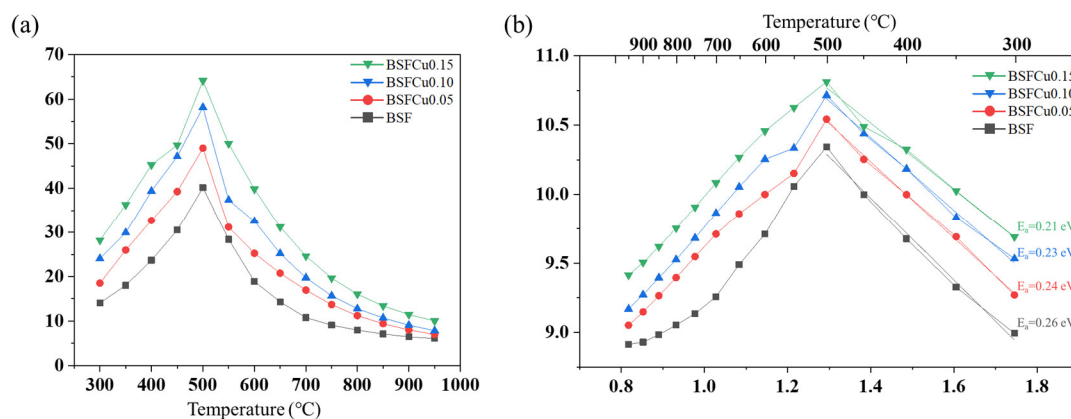


Figure 6. (a) The temperature dependence of electrical conductivity of the Ba_{0.5}Sr_{0.5}Fe_{1-x}Cu_xO_{3-δ} ($x = 0, 0.05, 0.10, 0.15$) measured from 300 °C to 950 °C in air; (b) $\ln(\sigma T)$ vs. $1000/T$ plot.

Figure 6b shows the Arrhenius plot for the electrical conductivity of BSFCu_x, and the relationship between electrical conductivity (σ) and temperature follows the Arrhenius equation [39]:

$$\sigma = A \exp\left(-\frac{E_a}{kT}\right) \quad (3)$$

where A , E_a , k , and T are the pre-exponential constant, activation energy, Boltzman constant, and temperature, respectively. According to the slope of linear fit over the temperature of 300–500 °C, the activation energy (E_a) was 0.26 eV ($x = 0$), 0.24 eV ($x = 0.05$), 0.23 eV ($x = 0.10$), and 0.21 eV ($x = 0.15$).

The low activation energy value helps to improve the hopping of the charge carrier, thereby increasing the electrical conductivity.

The cross-section view of the BSFCu0.15 | SDC | BSFCu0.15 symmetrical cell shows that the interface contact is tightly formed between the porous electrode and the dense electrolyte (Figure 7a). The ORR catalytic activity of BSFCu_x cathodes was assessed via electrochemical impedance spectroscopy of the symmetric cell configuration (BSFCu_x | SDC | BSFCu_x), and the EIS plots measured at 700 °C in air are shown in Figure 7b, where an ohmic resistance was subtracted. In order to clarify the ORR mechanism, the impedance spectra were fitted with the equivalent circuit model ($R_{HF} // CPE_{HF}$)-($R_{MF} // CPE_{MF}$)-($R_{LF} // CPE_{LF}$), which is inserted in Figure 7b. R and CPE in the parallel ($R // CPE$) represent the polarization resistance and constant phase element, respectively, and the corresponding results are displayed in Table 3.

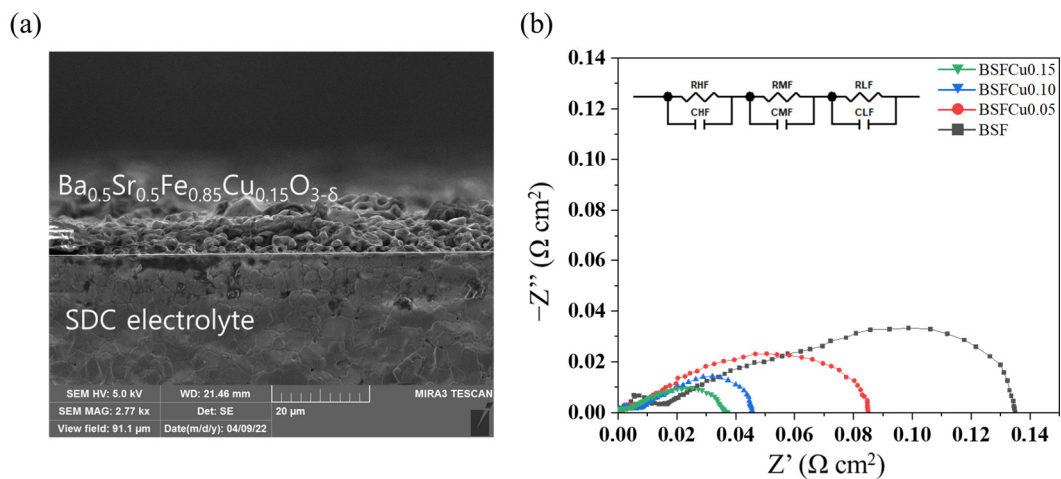


Figure 7. (a) Cross-section view of SEM image of the BSFCu0.15 | SDC | BSFCu0.15 symmetric cell; (b) impedance spectra of the BSFCu_x | SDC | BSFCu_x symmetric cell measured at 700 °C in air.

Table 3. The R_p fitting results of the Ba_{0.5}Sr_{0.5}Fe_{1-x}Cu_xO_{3-δ} ($x = 0, 0.05, 0.10, 0.15$) cathode at 700 °C.

Sample	R_{HF} (Ω)	R_{MF} (Ω)	R_{LF} (Ω)	R_p (Ω)	ASR ($\Omega \text{ cm}^2$)
BSF	0.141	0.285	0.529	0.955	0.135
BSFCu0.05	0.081	0.170	0.350	0.602	0.085
BSFCu0.10	0.073	0.100	0.145	0.318	0.045
BSFCu0.15	0.034	0.054	0.173	0.262	0.037

These impedance spectra consist of high-, medium-, and low-frequency arcs. In general, the high-frequency (HF) arc is related to the process of diffusion of oxygen ions from the triple-phase boundaries into the electrolyte, the medium-frequency (MF) arc is associated with the oxygen surface exchange, and the low-frequency (LF) arc is attributed to the gas diffusion process and oxygen adsorption–dissociation process [40]. In all cases, the low-frequency arc shows the highest polarization resistance, indicating that it was the rate-determining step of ORR. Among the three polarization resistances, R_{MF} decreased the most, by about 81%, from 0.285 Ω ($x = 0$) to 0.054 Ω ($x = 0.15$), and it is thought that this

is because the oxygen surface exchange reaction was accelerated by increasing the electron concentration of VB with Cu doping.

The area-specific resistance (ASR) can be calculated by measuring the distance between the intercepts of Z' or by using the equation as follows:

$$ASR = R_p \frac{\text{active area of cathode}}{2} \quad (4)$$

where $R_p = R_{HF} + R_{MF} + R_{LF}$ and the active area of the cathode is 0.2826 cm^2 . The ASR of the BSFCu x was $0.135 \text{ } \Omega \text{ cm}^2$ ($x = 0$), $0.085 \text{ } \Omega \text{ cm}^2$ ($x = 0.05$), $0.045 \text{ } \Omega \text{ cm}^2$ ($x = 0.10$), and $0.037 \text{ } \Omega \text{ cm}^2$ ($x = 0.15$). The BSFCu0.15 showed a 72.6% smaller value compared to that of BSF, which can be explained by higher oxygen vacancy concentration and electrical conductivity. A comparison of the ASRs for different iron-based electrodes is listed in Table 4. It can be concluded that the BSFCu0.15 cathode has high electrocatalytic activity for ORR due to improved interaction with adsorbed oxygen with an increase in oxygen vacancies at intermediate temperature.

Table 4. ASRs for different iron-based electrodes.

Cathode	Electrolyte	Operating Temperature (°C)	ASR ($\Omega \text{ cm}^2$)	Ref.
$\text{La}_{0.6}\text{Ca}_{0.4}\text{Fe}_{0.8}\text{Ni}_{0.2}\text{O}_{3-\delta}$	SDC	750	0.14	[41]
$\text{Bi}_{0.5}\text{Sr}_{0.5}\text{FeO}_{3-\delta}$	SDC	700	0.12	[42]
$\text{Sm}_{0.5}\text{Sr}_{0.5}\text{Fe}_{0.8}\text{Cu}_{0.2}\text{O}_{3-\delta}$	SDC	700	0.084	[43]
$\text{Ba}_{0.5}\text{Sr}_{0.5}\text{Fe}_{0.9}\text{Nb}_{0.1}\text{O}_{3-\delta}$	SDC	700	0.082	[44]
BSFCu0.15	SDC	700	0.037	This work

4. Conclusions

The oxygen reduction reaction (ORR) activity of a $\text{Ba}_{0.5}\text{Sr}_{0.5}\text{Fe}_{1-x}\text{Cu}_x\text{O}_{3-\delta}$ (BSFCu x , $x = 0, 0.05, 0.10, 0.15$) perovskite cathode was investigated. BSFCu x was crystallized into a cubic perovskite structure with a $Pm\bar{3}m$ space group, and it was confirmed that the lattice volume of the BSFCu x increased with Cu doping. For thermogravimetric and XPS analysis, the concentration of oxygen vacancies in the lattice increased with increasing Cu doping. The valence band maximum shifted from -0.133 eV ($x = 0$) to -0.222 eV ($x = 0.15$), which promoted the electron transfer from the cathode surface to adsorbed oxygen molecules. The electrical conductivity of BSFCu x increased with temperature by the thermally activated small polaron hopping mechanism, showing a maximum value of 64.12 S cm^{-1} ($x = 0.15$) at $500 \text{ }^\circ\text{C}$. The ASR of BSFCu0.15 was 72.6% smaller compared to that of BSF, which can be explained by higher oxygen vacancy concentration and electrical conductivity. The ORR activity of BSFCu x increased with Cu doping due to an increase in oxygen vacancy concentration and electron concentration in the valence band, which promotes electron exchange between the cathode surface and adsorbed oxygen.

Author Contributions: Conceptualization, T.L., K.J. and H.L.; Formal analysis, T.L.; Funding acquisition, H.L.; Investigation, T.L.; Methodology, T.L. and K.J.; Project administration, H.L.; Resources, H.L.; Writing—original draft, T.L. and K.J. All authors have read and agreed to the published version of the manuscript.

Funding: This work was supported by a 2-Year Research Grant of Pusan National University.

Institutional Review Board Statement: Not applicable.

Informed Consent Statement: Not applicable.

Data Availability Statement: Data available upon reasonable request.

Acknowledgments: This work was supported by a 2-Year Research Grant of Pusan National University.

Conflicts of Interest: The authors declare no conflict of interest.

References

1. Shao, Z.; Zhou, W.; Zhu, Z. Advanced synthesis of materials for intermediate-temperature solid oxide fuel cells. *Prog. Mater. Sci.* **2012**, *57*, 804–874. [[CrossRef](#)]
2. Mejía Gómez, A.E.; Sacanell, J.; Huck-Iriart, C.; Ramos, C.P.; Soldati, A.L.; Figueroa, S.J.A.; Tabacniks, M.H.; Fantini, M.C.A.; Craievich, A.F.; Lamas, D.G. Crystal structure, cobalt and iron speciation and oxygen non-stoichiometry of $\text{La}_{0.6}\text{Sr}_{0.4}\text{Co}_{1-y}\text{Fe}_y\text{O}_{3-\delta}$ nanorods for IT-SOFC cathodes. *J. Alloys Compd.* **2020**, *817*, 153250. [[CrossRef](#)]
3. Han, Z.; Bai, J.; Chen, X.; Zhu, X.; Zhou, D. Novel cobalt-free $\text{Pr}_2\text{Ni}_{1-x}\text{Nb}_x\text{O}_4$ ($x = 0, 0.05, 0.10, \text{ and } 0.15$) perovskite as the cathode material for IT-SOFC. *Int. J. Hydrogen Energy* **2021**, *46*, 11894–11907. [[CrossRef](#)]
4. Zan, J.; Wang, S.; Zheng, D.; Li, F.; Chen, W.; Pei, Q.; Jiang, L. Characterization and functional application of $\text{PrBa}_{0.5}\text{Sr}_{0.5}\text{Co}_{1.5}\text{Fe}_{0.5}\text{O}_{5+\delta}$ cathode material for IT-SOFC. *Mater. Res. Bull.* **2021**, *137*, 111173. [[CrossRef](#)]
5. Javed, M.S.; Shaheen, N.; Idrees, A.; Hu, C.; Raza, R. Electrochemical investigations of cobalt-free perovskite cathode material for intermediate temperature solid oxide fuel cell. *Int. J. Hydrogen Energy* **2017**, *42*, 10416–10422. [[CrossRef](#)]
6. Zhou, Q.; Gao, Y.; Wang, F.; An, D.; Li, Y.; Zou, Y.; Li, Z.; Wang, W. Novel cobalt-free cathode material $(\text{Nd}_{0.9}\text{La}_{0.1})_2(\text{Ni}_{0.74}\text{Cu}_{0.21}\text{Al}_{0.05})\text{O}_{4+\delta}$ for intermediate-temperature solid oxide fuel cells. *Ceram. Int.* **2015**, *41*, 639–643. [[CrossRef](#)]
7. Li, M.; Zhao, X.; Min, H.; Yuan, G.; Ding, X. Synergistically enhancing CO_2 -tolerance and oxygen reduction reaction activity of cobalt-free dual-phase cathode for solid oxide fuel cells. *Int. J. Hydrogen Energy* **2020**, *45*, 34058–34068. [[CrossRef](#)]
8. Wang, J.; Saccoccio, M.; Chen, D.; Gao, Y.; Chen, C.; Ciucci, F. The effect of A-site and B-site substitution on $\text{BaFeO}_{3-\delta}$: An investigation as a cathode material for intermediate-temperature solid oxide fuel cells. *J. Power Source* **2015**, *297*, 511–518. [[CrossRef](#)]
9. Sun, W.; Shi, Z.; Fang, S.; Yan, L.; Zhu, Z.; Liu, W. A high performance $\text{BaZr}_{0.1}\text{Ce}_{0.7}\text{Y}_{0.2}\text{O}_{3-\delta}$ -based solid oxide fuel cell with a cobalt-free $\text{Ba}_{0.5}\text{Sr}_{0.5}\text{FeO}_{3-\delta}-\text{Ce}_{0.8}\text{Sm}_{0.2}\text{O}_{2-\delta}$ composite cathode. *Int. J. Hydrogen Energy* **2010**, *35*, 7925–7929. [[CrossRef](#)]
10. Chen, C.; Chen, D.; Gao, Y.; Shao, Z.; Ciucci, F. Computational and experimental analysis of $\text{Ba}_{0.95}\text{La}_{0.05}\text{FeO}_{3-\delta}$ as a cathode material for solid oxide fuel cells. *J. Mater. Chem. A Mater. Energy Sustain.* **2014**, *2*, 14154–14163. [[CrossRef](#)]
11. Penwell, W.D.; Giorgi, J.B. Conductivity of cerium doped $\text{BaFeO}_{3-\delta}$ and applications for the detection of oxygen. *Sens. Actuators B Chem.* **2014**, *191*, 171–177. [[CrossRef](#)]
12. Roohandeh, T.; Saievar-Iranizad, E. Ni- and Cu-doping effects on formation and migration energies of oxygen vacancies in $\text{Ba}_{0.5}\text{Sr}_{0.5}\text{Fe}_{1-x}(\text{Cu}/\text{Ni})_x\text{O}_{3-\delta}$ perovskites: A DFT + U study. *Appl. Phys. A Mater. Sci. Process.* **2019**, *125*, 552. [[CrossRef](#)]
13. Gao, L.; Zhu, M.; Xia, T.; Li, Q.; Li, T.; Zhao, H. Ni-doped $\text{BaFeO}_{3-\delta}$ perovskite oxide as highly active cathode electrocatalyst for intermediate-temperature solid oxide fuel cells. *Electrochim. Acta* **2018**, *289*, 428–436. [[CrossRef](#)]
14. Lu, Y.; Zhao, H.; Chang, X.; Du, X.; Li, K.; Ma, Y.; Yi, S.; Du, Z.; Zheng, K.; Świerczek, K. Novel cobalt-free $\text{BaFe}_{1-x}\text{Gd}_x\text{O}_{3-\delta}$ perovskite membranes for oxygen separation. *J. Mater. Chem. A Mater. Energy Sustain.* **2016**, *4*, 10454–10466. [[CrossRef](#)]
15. Lu, J.; Yin, Y.-M.; Ma, Z.-F. Preparation and characterization of new cobalt-free cathode $\text{Pr}_{0.5}\text{Sr}_{0.5}\text{Fe}_{0.8}\text{Cu}_{0.2}\text{O}_{3-\delta}$ for IT-SOFC. *Int. J. Hydrogen Energy* **2013**, *38*, 10527–10533. [[CrossRef](#)]
16. Yin, J.-W.; Yin, Y.-M.; Lu, J.; Zhang, C.; Minh, N.Q.; Ma, Z.-F. Structure and properties of novel cobalt-free oxides $\text{Nd}_x\text{Sr}_{1-x}\text{Fe}_{0.8}\text{Cu}_{0.2}\text{O}_{3-\delta}$ ($0.3 \leq x \leq 0.7$) as cathodes of intermediate temperature solid oxide fuel cells. *J. Phys. Chem. C Nanomater. Interfaces* **2014**, *118*, 13357–13368. [[CrossRef](#)]
17. Niemczyk, A.; Zheng, K.; Cichy, K.; Berent, K.; Küster, K.; Starke, U.; Poudel, B.; Dabrowski, B.; Świerczek, K. High Cu content $\text{LaNi}_{1-x}\text{Cu}_x\text{O}_{3-\delta}$ perovskites as candidate air electrode materials for Reversible Solid Oxide Cells. *Int. J. Hydrogen Energy* **2020**, *45*, 29449–29464. [[CrossRef](#)]
18. Lach, J.; Zheng, K.; Kluczowski, R.; Niemczyk, A.; Zhao, H.; Chen, M. Tuning Cu-Content $\text{La}_{1-x}\text{Sr}_x\text{Ni}_{1-y}\text{Cu}_y\text{O}_{3-\delta}$ with Strontium Doping as Cobalt-Free Cathode Materials for High-Performance Anode-Supported IT-SOFCs. *Materials* **2022**, *15*, 8737. [[CrossRef](#)]
19. Fitriana, F.; Baity, P.S.N.; Zainuri, M.; Kidkhunthod, P.; Suasmoro, S. Crystal structure and Cu/Fe K-edge analysis of $\text{Ba}_{0.5}\text{Sr}_{0.5}\text{Fe}_{1-x}\text{Cu}_x\text{O}_{3-\delta}$ ($x = 0-0.2$) and the influence on conductivity. *J. Phys. Chem. Solids* **2021**, *154*, 110065. [[CrossRef](#)]
20. Ishihara, T. (Ed.) *Perovskite Oxide for Solid Oxide Fuel Cells*, 2009th ed.; Springer: New York, NY, USA, 2014.
21. Hardin, W.G.; Mefford, J.T.; Slanac, D.A.; Patel, B.B.; Wang, X.; Dai, S.; Zhao, X.; Ruoff, R.S.; Johnston, K.P.; Stevenson, K.J. Tuning the electrocatalytic activity of perovskites through active site variation and support interactions. *Chem. Mater.* **2014**, *26*, 3368–3376. [[CrossRef](#)]
22. Jung, N.; Sohn, Y.; Park, J.H.; Nahm, K.S.; Kim, P.; Yoo, S.J. High-performance $\text{PtCu}_x@Pt$ core-shell nanoparticles decorated with nanoporous Pt surfaces for oxygen reduction reaction. *Appl. Catal. B* **2016**, *196*, 199–206. [[CrossRef](#)]
23. Zhu, Z.; Shi, Y.; Aruta, C.; Yang, N. Improving electronic conductivity and oxygen reduction activity in Sr-doped lanthanum cobaltite thin films: Cobalt valence state and electronic band structure effects. *ACS Appl. Energy Mater.* **2018**, *1*, 5308–5317. [[CrossRef](#)]
24. Mushtaq, N.; Lu, Y.; Xia, C.; Dong, W.; Wang, B.; Wang, X.; Shah, M.A.K.Y.; Rauf, S.; Nie, J.; Hu, E.; et al. Design principle and assessing the correlations in Sb-doped $\text{Ba}_{0.5}\text{Sr}_{0.5}\text{FeO}_{3-\delta}$ perovskite oxide for enhanced oxygen reduction catalytic performance. *J. Catal.* **2021**, *395*, 168–177. [[CrossRef](#)]
25. Wang, Z.; Lv, P.; Yang, L.; Guan, R.; Jiang, J.; Jin, F.; He, T. $\text{Ba}_{0.95}\text{La}_{0.05}\text{Fe}_{0.8}\text{Zn}_{0.2}\text{O}_{3-\delta}$ cobalt-free perovskite as a triple-conducting cathode for proton-conducting solid oxide fuel cells. *Ceram. Int.* **2020**, *46*, 18216–18223. [[CrossRef](#)]

26. Meng, F.; Xia, T.; Wang, J.; Shi, Z.; Lian, J.; Zhao, H.; Bassat, J.-M.; Grenier, J.-C. Evaluation of layered perovskites $\text{YBa}_{1-x}\text{Sr}_x\text{Co}_2\text{O}_{5+\delta}$ as cathodes for intermediate-temperature solid oxide fuel cells. *Int. J. Hydrogen Energy* **2014**, *39*, 4531–4543. [[CrossRef](#)]
27. Liu, B.; Zhang, Y.; Tang, L. X-ray photoelectron spectroscopic studies of $\text{Ba}_{0.5}\text{Sr}_{0.5}\text{Co}_{0.8}\text{Fe}_{0.2}\text{O}_{3-\delta}$ cathode for solid oxide fuel cells. *Int. J. Hydrogen Energy* **2009**, *34*, 435–439. [[CrossRef](#)]
28. Yao, C.; Yang, J.; Zhang, H.; Meng, J.; Meng, F. Cobalt-free perovskite $\text{SrTa}_{0.1}\text{Mo}_{0.1}\text{Fe}_{0.8}\text{O}_{3-\delta}$ as cathode for intermediate-temperature solid oxide fuel cells. *Int. J. Energy Res.* **2020**, *44*, 925–933. [[CrossRef](#)]
29. Sun, Q.; Sun, L.; Dou, Y.; Li, Q.; Li, N.; Huo, L.; Zhao, H. Insights into the oxygen reduction reaction on Cu-doped $\text{SrFeO}_{3-\delta}$ cathode for solid oxide fuel cells. *J. Power Source* **2021**, *497*, 229877. [[CrossRef](#)]
30. Yao, C.; Yang, J.; Chen, S.; Meng, J.; Cai, K.; Zhang, Q. Copper doped $\text{SrFe}_{0.9-x}\text{CuW}_{0.1}\text{O}_{3-\delta}$ ($x = 0-0.3$) perovskites as cathode materials for IT-SOFCs. *J. Alloys Compd.* **2021**, *868*, 159127. [[CrossRef](#)]
31. Lim, C.; Yang, Y.; Sin, Y.-W.; Choi, S.; Kim, G. Ca- and Ni-doped $\text{pr}_{0.5}\text{Ba}_{0.5}\text{FeO}_{3-\delta}$ as a highly active and robust cathode for high-temperature solid oxide fuel cell. *Energy Fuels* **2020**, *34*, 11458–11463. [[CrossRef](#)]
32. Yao, C.; Zhang, H.; Liu, X.; Meng, J.; Meng, F. A niobium and tungsten co-doped $\text{SrFeO}_{3-\delta}$ perovskite as cathode for intermediate temperature solid oxide fuel cells. *Ceram. Int.* **2019**, *45*, 7351–7358. [[CrossRef](#)]
33. Yao, C.; Meng, J.; Liu, X.; Zhang, X.; Meng, F.; Wu, X.; Meng, J. Effects of Bi doping on the microstructure, electrical and electrochemical properties of $\text{La}_{2-x}\text{Bi}_x\text{Cu}_{0.5}\text{Mn}_{1.5}\text{O}_6$ ($x = 0, 0.1$ and 0.2) perovskites as novel cathodes for solid oxide fuel cells. *Electrochim. Acta* **2017**, *229*, 429–437. [[CrossRef](#)]
34. Wu, Y.; Li, K.; Yang, Y.; Song, W.; Ma, Z.; Chen, H.; Ou, X.; Zhao, L.; Khan, M.; Ling, Y. Investigation of Fe-substituted in $\text{BaZr}_{0.8}\text{Y}_{0.2}\text{O}_{3-\delta}$ proton conducting oxides as cathode materials for protonic ceramics fuel cells. *J. Alloys Compd.* **2020**, *814*, 152220. [[CrossRef](#)]
35. Pramana, S.S.; Cavallaro, A.; Li, C.; Handoko, A.D.; Chan, K.W.; Walker, R.J.; Regoutz, A.; Herrin, J.S.; Yeo, B.S.; Payne, D.J.; et al. Crystal structure and surface characteristics of Sr-doped $\text{GdBaCo}_2\text{O}_{6-\delta}$ double perovskites: Oxygen evolution reaction and conductivity. *J. Mater. Chem. A Mater. Energy Sustain.* **2018**, *6*, 5335–5345. [[CrossRef](#)]
36. Marasi, M.; Panunzi, A.P.; Duranti, L.; Lisi, N.; Di Bartolomeo, E. Enhancing oxygen reduction activity and structural stability of $\text{La}_{0.6}\text{Sr}_{0.4}\text{FeO}_{3-\delta}$ by 1 mol % Pt and Ru B-site doping for application in all-perovskite IT-SOFCs. *ACS Appl. Energy Mater.* **2022**, *5*, 2918–2928. [[CrossRef](#)]
37. Xie, D.; Guo, W.; Guo, R.; Liu, Z.; Sun, D.; Meng, L.; Zheng, L.; Wang, B. Synthesis and electrochemical properties of $\text{BaFe}_{1-x}\text{Cu}_x\text{O}_{3-\delta}$ Perovskite oxide for IT-SOFC cathode. *Fuel Cells* **2016**, *16*, 829–838. [[CrossRef](#)]
38. Sun, W.; Yan, L.; Zhang, S.; Liu, W. Crystal structure, electrical conductivity and sintering of $\text{Ba}_{0.5}\text{Sr}_{0.5}\text{Zn}_x\text{Fe}_{1-x}\text{O}_{3-\delta}$. *J. Alloys Compd.* **2009**, *485*, 872–875. [[CrossRef](#)]
39. Wei, Z.; Li, Z.; Wang, Z.; Zhao, Y.; Wang, J.; Chai, J. A free-cobalt barium ferrite cathode with improved resistance against CO_2 and water vapor for protonic ceramic fuel cells. *Int. J. Hydrogen Energy* **2022**, *47*, 13490–13501. [[CrossRef](#)]
40. Li, H.; Lü, Z. A highly stable cobalt-free $\text{LaBa}_{0.5}\text{Sr}_{0.5}\text{Fe}_2\text{O}_{6-\delta}$ oxide as a high performance cathode material for solid oxide fuel cells. *Int. J. Hydrogen Energy* **2020**, *45*, 19831–19839. [[CrossRef](#)]
41. Yang, G.; Su, C.; Chen, Y.; Tadé, M.O.; Shao, Z. Nano $\text{La}_{0.6}\text{Ca}_{0.4}\text{Fe}_{0.8}\text{Ni}_{0.2}\text{O}_{3-\delta}$ decorated porous doped ceria as a novel cobalt-free electrode for “symmetrical” solid oxide fuel cells. *J. Mater. Chem. A Mater. Energy Sustain.* **2014**, *2*, 19526–19535. [[CrossRef](#)]
42. Niu, Y.; Zhou, W.; Sunarso, J.; Ge, L.; Zhu, Z.; Shao, Z. High performance cobalt-free perovskite cathode for intermediate temperature solid oxide fuel cells. *J. Mater. Chem.* **2010**, *20*, 9619–9622. [[CrossRef](#)]
43. Ling, Y.; Zhao, L.; Lin, B.; Dong, Y.; Zhang, X.; Meng, G.; Liu, X. Investigation of cobalt-free cathode material $\text{Sm}_{0.5}\text{Sr}_{0.5}\text{Fe}_{0.8}\text{Cu}_{0.2}\text{O}_{3-\delta}$ for intermediate temperature solid oxide fuel cell. *Int. J. Hydrogen Energy* **2010**, *35*, 6905–6910. [[CrossRef](#)]
44. Huang, S.; Wang, G.; Sun, X.; Lei, C.; Li, T.; Wang, C. Cobalt-free perovskite $\text{Ba}_{0.5}\text{Sr}_{0.5}\text{Fe}_{0.9}\text{Nb}_{0.1}\text{O}_{3-\delta}$ as a cathode material for intermediate temperature solid oxide fuel cells. *J. Alloys Compd.* **2012**, *543*, 26–30. [[CrossRef](#)]

Disclaimer/Publisher’s Note: The statements, opinions and data contained in all publications are solely those of the individual author(s) and contributor(s) and not of MDPI and/or the editor(s). MDPI and/or the editor(s) disclaim responsibility for any injury to people or property resulting from any ideas, methods, instructions or products referred to in the content.